RESEARCH ARTICLE

Magnetic Field-Based Induction Machine Modeling Incorporating Space and Time Harmonic Effects

BUDDHIKA DE SILVA GURUWATTA VIDANALAGE [ID][1]**, (Graduate Student Member, IEEE),**
ANTHONY LOMBARDI[2]**, JIMI TJONG**[1]**, AND NARAYAN C. KAR**[1]**, (Senior Member, IEEE)**
[1]Centre for Hybrid Automotive Research & Green Energy (CHARGE), University of Windsor, Windsor, ON N9B 3P4, Canada
[2]Nemak, Windsor, ON N9C 4G8, Canada

Corresponding author: Buddhika De Silva Guruwatta Vidanalage (guruwat@uwindsor.ca)

ABSTRACT Integration of the impacts of time and space harmonics simultaneously during the design stages of inverter-fed induction machines (IMs) is crucial for the accurate calculation of electromagnetic (EM) torque and ripples. Traditional magnetic field-based models offer an analytical approach for determining the EM torque in IMs by calculating inductances. However, by assuming infinite core permeabilities, these models neglect the impact of the core magnetomotive force (MMF) drops due to the difficulties in accurately calculating these drops and the impracticality of isolating the contribution from each phase, which is essential for inductances calculations. These factors contribute to deficiencies in this modeling approach, which become more noticeable when the combined impacts of time and space harmonics on MMF drop calculations are also disregarded. Therefore, this paper introduces a novel magnetic-field-based model to predict the torque and torque ripples of inverter-fed induction motors by addressing the above limitations. This involves modifying the turns and winding function, and calculating the core MMF drops based on the timely variation of non-sinusoidal core flux densities, considering their major and minor flux-density loop effects. Consequently, the associated energy is used to calculate the net available energy, thereby enhancing torque calculations. Compared to the experimental results obtained from an 11kW prototyped induction motor, the proposed model exhibits notable enhancements, achieving average accuracies of 96.4% for average torque and 94.51% for torque ripples, in contrast to the respective traditional model accuracies, 81.1% and 45.1%.

INDEX TERMS Induction machine, magnetomotive force drops, minor flux density loops, pulse width modulation, space harmonics, time harmonics, winding function.

I. INTRODUCTION

There is a growing interest in employing high-performance electric motors such as induction motors in electric vehicles (EVs) applications due to their lower cost; robust structure; wider operating speed range; and higher reliability [1]. These motors can serve as a practical solution for small and regular EVs, such as electric micro cars and three-wheelers, utilizing small traction electric motors (e-motors) with power

The associate editor coordinating the review of this manuscript and approving it for publication was Lei Zhao [ID].

ratings between 7 to 15 kW [2] and Audi e-tron 140 kW [3]. However, induction motors have lower power and torque density and efficiency as compared to permanent magnet synchronous motors [4].

The power and torque versus speed characteristics of traction motors play a critical role in influencing the operating performance of EVs [5]. The inclusion of integrated pulse-width modulation (PWM) inverters within the EV drive system introduces additional time harmonics, which when combined with space harmonics, negatively affect the electromagnetic performance [6], [7]. Therefore, it becomes

necessary to consider the effects of time and space harmonics during the induction machine design stage to improve electromagnetic torque performance across the entire speed range.

2D/3D finite element analysis (FEA) is traditionally used to accurately calculate induction motor performance. However, FEA is a computationally intensive approach, rendering it impractical for rapid exploration and iteration, especially during the initial machine design phases. Therefore, there is a need for an alternative, a computationally efficient yet accurate magnetic field-based analytical model that can be employed during the initial design and optimization stages [8], [9]. Analytical models, such as the magnetic equivalent circuit model [10], subdomain model [11], and Fourier-based model [12] produce reasonably accurate results. However, they are not ideal for the initial design stages due to their heavy reliance on complex geometric information that is not readily available during the initial motor design stages and leads to inaccurate electromagnetic performance calculations.

The other analytical models [13], [14], [15], [16], [17] are based on winding function (WF) and the physical geometry of the induction motor. These methods yield a detailed insight into motor behavior and have a relatively low computational burden. These models use instantaneous rotor-position-dependent inductances and are dependent on the airgap flux density and its space harmonics. However, assumptions of infinite magnetic permeabilities of the magnetic cores and idealized winding distributions led traditional WF models to overestimate the airgap flux densities and inductances, thereby negatively impacting the electromagnetic torque calculation accuracy [6], [18].

Consequently, despite various efforts to account for space harmonics through methods such as permeance differences caused by stator and rotor slot openings [13], [19], [20], and utilize stepped variations in winding functions [13], [14], [15], [16], [17], it is important that all these models share a common assumption of infinite permeability thereby neglecting their impact on space harmonics. Furthermore, the models reported in [6] and [7] attempted to address the significance of non-sinusoidal excitations. However, the focus was primarily limited to the combined effects of time and space harmonics arising from the winding layout while neglecting the core magnetomotive force (MMF) drops.

The traditional WF models reported in [8], [21], and [22] use the saturation factor to consider saturation effects due to the stator tooth tip areas calculated based on the full and no-load airgap voltages. The airgap length is changed based on the saturation factor to account for the core MMF drops. This single saturation factor approach fails to appropriately account for the core saturation in the different sections of the machine and related core MMF drops. Furthermore, the practicality of discretizing the individual stator phases and rotor effects after considering the combined core MMF drops in different sections for use in inductance calculations is questionable. In addition, traditional WF models only consider a saturation factor at the rated operating speed of machines.

Moreover, the time harmonics contribute to the additional MMF drops within the core regions, especially due to the core saturation. Since traditional WF models are primarily designed for sinusoidal excitations and are not optimal for operating with non-sinusoidal inputs, the additional core MMF drops due to the time harmonics are neglected [23]. As a result, this compromises the accuracy of torque calculations in traditional WF models and is more pronounced when they are applied to compute the torque in traction induction machines powered by PWM inverters. Therefore, it can be concluded that a computationally efficient magnetic field-based model is required to precisely predict the torque characteristics of the traction induction motors, particularly during their initial designing stages. The model should:

(a) Consider the simultaneous combined effects of time harmonics and space harmonics.
(b) Integrate core MMF drops considering the timely variation of core flux densities.
(c) Be able to estimate the torque including its torque ripples in both maximum torque per amp (MTPA) and field weakening (FW) operating regions.

Therefore, this work proposes a magnetic field-based model for small-scale traction induction motors to calculate the average torque including its ripples considering the points mentioned above particularly to be used at their initial designing stages.

II. ELECTROMAGNETIC TORQUE CALCULATION USING THE TRADITIONAL WINDING FUNCTION MODEL

Through comprehension, the space harmonics content in the airgap flux density has a high correlation to the quality of the steady-state torque by producing parasitic torques [8]. Therefore, accurate integration of the space harmonics in the proposed model is important for torque and its ripple calculation as per the paper's objectives.

As per the WF theory, the winding pattern is integrated into the modeling by taking the aggregated winding turns distribution of each phase along the circumference of the motor considering the direction of the currents in each winding turn, named as the turns function, $\lambda_{turn}(\alpha_s)$, and the winding function, $\lambda_{win}(\alpha_s, \alpha_r)$, is then derived according to (1). Where, "α_s" is the electrical angle along the stator, and "α_r" is the rotor movement angle referred to the fixed stator reference axis.

$$\lambda_{win}(\alpha_s, \alpha_r) = \lambda_{turn}(\alpha_s) - \frac{1}{P\pi \left\langle \Delta_{eff}^{-1}(\alpha_s, \alpha_r) \right\rangle} \int_0^{P\pi} \lambda_{turn}(\alpha_s)$$
$$\times \Delta_{eff}^{-1}(\alpha_s, \alpha_r) \, d\alpha_s \qquad (1)$$

where, P and $\Delta_{eff}(\alpha_s, \alpha_r)$ represent the number of poles and the effective airgap length function respectively and the net MMF generated at the windings [$\Lambda_{win}(\alpha_s, \alpha_r, t)$] are calculated by summing up the MMF generated by each phase and

as shown in (2) [20]:

$$\Lambda_{win}(\alpha_s, \alpha_r, t) = \sum_{\xi=phase} \lambda_{win,\xi}(\alpha_s, \alpha_r) \times i_\xi(t) \quad (2)$$

In this context, phase current, $i_\xi(t)$ exhibits a 120^0 of electrical degree phase difference between each other within the three-phase system. Under the initial assumption of traditional WF models, the absence of MMF core drops results in the net MMF generated at the windings appearing at the airgap in the radial direction and used for the calculation of the airgap flux density distribution, $B_{ag}(\alpha_s, \alpha_r, t)$ as shown in (3) [20]:

$$B_{ag}(\alpha_s, \alpha_r, t) = \frac{(4\pi \times 10^{-7}) \times \Lambda_{win}(\alpha_s, \alpha_r, t)}{\Delta_{eff}(\alpha_s, \alpha_r)} \quad (3)$$

In traditional WF models, the airgap's anisotropic configuration and the slotting effects, are addressed by modeling the non-slot areas of the machine and the effective airgap length function according to (4) by modifying the airgap length through Carter factor (C_{factor}) for the average core saturation and slotting effects [8], [13]:

$$\begin{rcases} C_{factor} = \tau_s / \left[(\tau_s - b_{so}) + \frac{4g}{\pi} \ln(1 + \frac{\pi b_{so}}{4g}) \right] \\ g_{eff} = (\frac{g}{2}) \times C_{factor} \\ \Delta_{eff\_stator}(\alpha_s) = g_{eff} \quad \alpha_s \forall \text{ stator smooth airgap areas} \\ \Delta_{eff\_stator}(\alpha_s) = g_{eff} + h_{ts} \quad \alpha_s \in \text{ stator slot opening} \\ \Delta_{eff\_rotor}(\alpha_s, \alpha_r) = g_{eff} \quad \alpha_s \forall \text{ rotor smooth airgap areas} \\ \Delta_{eff\_rotor}(\alpha_s, \alpha_r) = g_{eff} + h_{tr} \quad \alpha_s \in \text{ rotor slot opening} \\ \Delta_{eff}(\alpha_s, \alpha_r) = \Delta_{eff\_stator}(\alpha_s) + \Delta_{eff\_rotor}(\alpha_s, \alpha_r) \end{rcases} \quad (4)$$

where τ_s, b_{so}, g, h_{ts} and h_{tr} represent the slot pitch, slot opening, actual airgap length, and stator and rotor teeth heights respectively and "α_r" is related to the stator excitation frequency (f_s) and the operational slip (s) as shown in (5):

$$\alpha_r = 2\pi f_s (1 - s)t \quad (5)$$

Then $B_{ag}(\alpha_s, \alpha_r, t)$ is used to calculate the differential magnetic flux across the air gap in the radial direction from stator to rotor through the flux tubes while the magnetizing inductances, self- and mutual-inductances of i and j circuits are calculated based on (6) [8], [19], [21], [22]. Furthermore, the rotor winding functions of the squirrel-cage induction motor (SCIM) can be developed by considering the rotor mesh loops comprising two closely positioned bars with ring segments connecting them and regarding the rotor loop as a single-turn coil and using (1):

$$L_{ij}(\alpha_r) = 4\pi \times 10^{-7} \cdot l_s \cdot r_{ag} \int_0^{P\pi}$$
$$\times \frac{\lambda_{win,j}(\alpha_s, \alpha_r) \cdot \lambda_{turn,i}(\alpha_s, \alpha_r)}{\Delta_{eff}(\alpha_s, \alpha_r)} d\alpha_s \quad (6)$$

where l_s and r_{ag} represent the stack length and airgap radius, respectively. The calculated magnetizing inductances of stator phase windings and rotor mesh loops are denoted by subscripts "s" and "r", respectively, based on (6) used to formulate the four inductance matrices: $\mathbf{L}_{ss}$, $\mathbf{L}_{rr}$, $\mathbf{L}_{sr}$, $\mathbf{L}_{rs}$ and where $\mathbf{L}_{rs} = \mathbf{L}_{sr}^{\mathrm{T}}$. The additional slot leakage inductances are added to the diagonal elements of $\mathbf{L}_{ss}$ and calculated as in [13]. Therefore, the magnetic energy conversion principles can be used to evaluate the torque (τ_{em}) as shown in (7) [19].

$$\begin{rcases} \tau_{em} = \frac{1}{2} \cdot \frac{P}{2} \cdot \frac{\partial W_{coe}(\alpha_r, i(t))}{\partial \alpha_r} \\ W_{coe}(\alpha_r, i(t)) = \begin{pmatrix} i_s(t) \\ i_r(t) \end{pmatrix}^T \cdot \begin{pmatrix} \mathbf{L}_{ss}(\alpha_r) & \mathbf{L}_{sr}(\alpha_r) \\ \mathbf{L}_{rs}(\alpha_r) & \mathbf{L}_{rr}(\alpha_r) \end{pmatrix} \cdot \begin{pmatrix} i_s(t) \\ i_r(t) \end{pmatrix} \end{rcases}$$
$$(7)$$

where $[i_s]_{3\times1}$ and $[i_r]_{N_r\times1}$ represent the stator and rotor mesh loop current matrices, respectively, and N_r is the number of rotor mesh loops.

III. DEVELOPMENT STEPS OF THE PROPOSED MODEL

The accuracy of the torque calculation, as in (7), primarily depends on the quality of the calculated inductances and stator and rotor currents, which are unknown variables that vary depending on the voltage excitation, as in (8) [19].

$$\begin{rcases} \overline{v_s} = \mathrm{R}_s \, \overline{i_s} + \frac{d}{dt}[\mathbf{L}_{ss}(\alpha_r) \cdot \overline{i_s} + \mathbf{L}_{sr}(\alpha_r) \cdot \overline{i_r}] \\ 0 = \mathrm{R}_r \, \overline{i_r} + \frac{d}{dt}[\mathbf{L}_{sr}^T(\alpha_r) \cdot \overline{i_s} + \mathbf{L}_{rr}(\alpha_r) \cdot \overline{i_r}] \end{rcases} \quad (8)$$

where $[\mathbf{R}_s]_{3\times3}$, $[\mathbf{R}_r]_{N_r\times N_r}$ and $[v_s]_{3\times1}$ are the matrices of stator and rotor resistance, and stator phase voltages respectively. According to (6), the inductances are influenced by their spatial harmonic content, which is affected by three main factors: (i) winding layout; (ii) presence of stator slotting effects; and (iii) presence of rotor slotting effects. The spatial harmonics in the winding layout are closely related to the chosen winding pattern, while stator slot openings contribute additional space harmonics (S_{sh}) in the order of ($2kQ_s\pm1$), and the rotor movement causes time-variant rotor slot harmonics (S_{rh}) due to the permeance variations in the order of ($2kQ_r\pm1$). Here, Q_s and Q_r represent the number of stator and rotor slots per pole, respectively, and k is a positive integer.

Furthermore, as per (8), the space harmonics introduce time harmonics in the stator currents, and the situation becomes even more intricate when PWM non-sinusoidal voltage excitations are involved since non-sinusoidal currents lead to non-sinusoidal core flux densities resulting in time-dependent core MMF drops that affect the torque and torque ripples differently leading to various parasitic effects. Consequentially, traditional WF models, which rely on sinusoidal currents, typically overlook these additional parasitic effects resulting in significantly lower accuracies.

Therefore, the proposed model aims to address the PWM time harmonics effects on the torque calculation of the induction motors considering the parasitic effects due to the interactions between space harmonics mainly originating from the winding layout and the core MMF drops. Furthermore, the primary focus of this model is to facilitate designers during the initial design stages of traction induction motors for EVs.

A. WINDING FUNCTION MODELING CONSIDERING SPACE HARMONICS AND INTERACTION WITH TIME HARMONICS

In reference to (1)–(5), the precise representation of the stator winding and turn function is necessary to encounter their space harmonic effects. These space harmonics can be attributed to the following principal factors:

- Induction motor's stator winding layout.
- Stator slot geometry, number of stator slots and poles.

The use of Ampere's law in developing the turn and winding functions leads to distinct variations in the slot openings based on the winding turns present in neighboring slots. Traditionally, it is presumed that these turns were uniformly spread across the width of the slot openings [19], when openings are not very small. Therefore, the turn distribution changes with the choice of the slot opening, irrespective of the slot geometry or winding arrangement. However, during the initial design phase, the stator slots were designed to conform to the permissible standard slot fill factor values while determining the required number of conductors and their sizes based on the current density values. As a result, the conductors are distributed throughout the stator slots rather than being assumed to be concentrated solely at the slot opening areas. Consequently, to formulate the turn and winding functions accurately, it is more precise to consider the actual occupied area of the phase windings (A_{con}), which is distributed within the slot. Therefore, a modification is proposed to the step changes occurring at the slot opening area by considering the virtual winding-occupied area as a rectangular shape, as shown in Fig. 1. The height of this rectangular shape matches the slot height (l_{sh}), and its width (l_w) is calculated using (9). Here, within this l_w area, the turns and winding functions exhibit a linear variation as in Fig. 1:

$$A_{con} = (\pi d^2/4) \times N_{ph\_sl} \ and \ l_w = A_{con}/l_{sh} \quad (9)$$

where d and N_{ph_sl} represent the diameter of the single conductor and the number of conductors per slot. Hence, a quantitative assessment of the efficiency of the suggested adjustments to the turn and winding function is executed based on the four-pole induction motor with 36 stator slots and 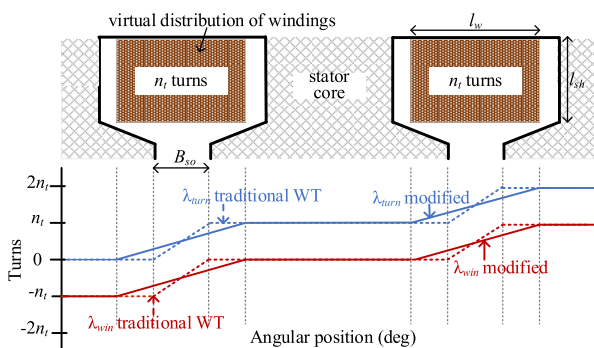12 conductors per slot and employing distributed windings and the evaluated fundamental and overall harmonic distortion of the winding functions of each phase under two different slot opening conditions. This is compared with the outcomes obtained through FEA results as shown in Fig. 2. Where to analyze the space harmonics solely due to the winding arrangement, the analyses are conducted as follows:

- Smooth stator and rotor surfaces.
- Eliminated the influence of core MMF drops.

As depicted in Fig. 2, the accuracy of the proposed techniques in predicting the fundamental winding MMF stands at 99.9%, with an average accuracy of 91% for higher-order harmonics compared to FEA results of a similar induction motor with two different stator slot opening lengths. However, in conventional WF approach the above accuracies are reported as 97% and 78%, respectively.
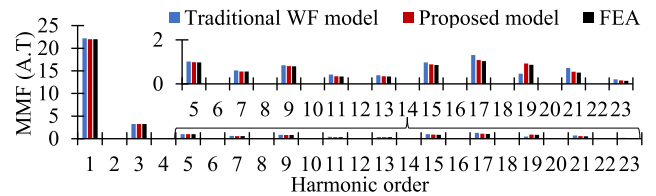

FIGURE 2. Comparison of the space harmonics of the winding MMFs due to the conventional and proposed approaches compared with the FEA results.

The analysis of harmonics, including space harmonics influenced by the winding function and time harmonics influenced by the sinusoidal PWM inverter, can be conducted corresponding to their waveforms, as depicted in Fig. 3. Accordingly, the winding function of each phase, along with their combined waveform and the PWM line/phase voltages, demonstrates a symmetrical distribution across the positive and negative halves of a cycle. Consequently, the second-order harmonics are uniformly distributed across both halves, leading to their combined effect summing to zero according to Fourier transform theories. Hence, second-order harmonics are absent from the winding function, PWM voltage, and input current waveforms of IMs under healthy conditions.
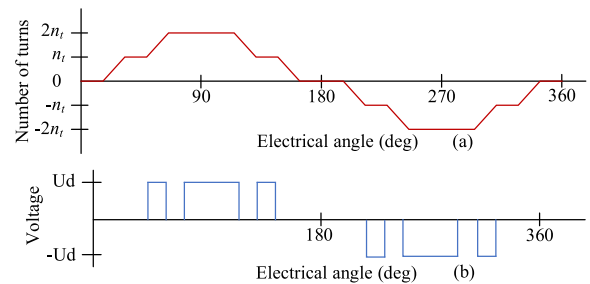

FIGURE 3. Symmetrically distributed waveforms. (a) Winding function distribution of single-phase in one pole pair. (b) Line voltage of sinusoidal PWM inverter output.

Furthermore, space harmonics due to the winding functions of each phase are in the order of triplen (3rd and 9th are more dominant), ($6h \pm 1$) [h's = 0, 1, 2 are more influential] and the space harmonics due to the stator slotting

FIGURE 1. Stator winding and turns functions of single phase winding: conventional vs modified versions.

effects. However, the symmetrical arrangement of the stator phase windings with 120^0(electrical degrees) displacement resulted in the combined winding function waveform with eliminated triplen harmonics. Conversely, the six-step PWM inverters generate time harmonics in the order of the $(6n \pm 1)$, where n is a positive integer, the harmonic orders; 1st, 5th, 7th, 11th, and 13th are more dominant and the eliminated triplen harmonics effects followed by symmetrically displaced three-phase currents by 120 degrees, when connected to IMs running under healthy conditions [24].

Hence, during the initial design phases of electric motors, it is necessary to account for the cumulative impacts of winding space harmonics and the more significant PWM current harmonics and space harmonic orders mentioned earlier. Consequently, the resulting airgap MMF can be determined by referencing the three-phase induction motor, as depicted in (10). Additionally, it is important to note that this modeling approach is not restricted solely to the specified current harmonic orders. Designers have the flexibility to incorporate higher-order harmonics according to their preferences.

$$
\left.\begin{aligned}
\lambda_{win,A}(\alpha_s) &= \sum_{\beta=1,3,5,7,9,11,13,S_{sh}} N_\beta \cos(\beta\alpha_s) \\
\lambda_{win,B}(\alpha_s) &= \lambda_{win,A}(\alpha_s - \tfrac{2\pi}{3}) \\
\lambda_{win,C}(\alpha_s) &= \lambda_{win,A}(\alpha_s + \tfrac{2\pi}{3}) \\
i_{ph,\xi}(t) &= \sum_{\chi=1,5,7,11,13} I_{m,\chi} \cos[\chi(\omega_s t + \gamma_\xi)] \\
\Lambda_{win}(\alpha_s,t) &= \sum_{\xi=A,B,C} \sum_{\chi=1,5,7,11,13} \lambda_{win,\xi,\chi}(\alpha_s) \\
&\quad \cdot I_{m,\chi} \cos[\chi(\omega_s t + \gamma_\xi)]
\end{aligned}\right\}
$$
(10)

where N_β and $I_{m,\chi}$ denote the peak magnitudes of the winding function and phase currents of the βth space and χ^{th} time harmonics respectively.

Additionally, γ_ξ signifies the phase shifts of $(2\pi/3)$ radians between the three-phase currents. Given the fixed and predetermined nature of the machine's winding function, the influence of individual time harmonics on the airgap MMF is determined through the superposition principle which involves analyzing the impact of each current harmonic $[i_{ph,\xi}(t)]$ separately. Therefore, according to (10), the individual significant time harmonics interact with the significant space harmonics to generate the net MMF waveform. The resultant space harmonics of the MMF waveform are due to the fundamental time harmonic with their respective phase sequences indicating forward or reverse rotation. The synchronous speeds of the space harmonics relative to the fundamental time harmonics and their corresponding synchronous speeds relative to the fundamental harmonic are depicted in Fig. 4.

In Fig. 4(a), individual space harmonics are depicted as creators of corresponding poles based on their harmonic order and are equal to the harmonic order times the machine poles. While maintaining a constant number of winding turns per phase (N_{Tph}), the winding turns per pole (N_{thp}) of the βth higher order space harmonics can be calculated using (11),
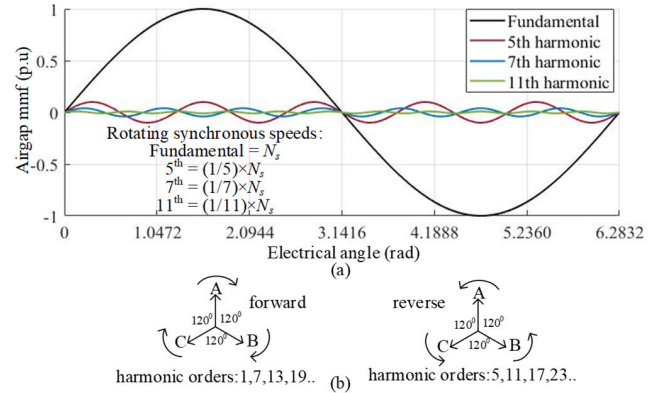

FIGURE 4. Airgap MMF waveform in one pole pair due to fundamental time harmonic. (a) Space harmonics and their synchronous speeds. (b) Phase sequences of different space harmonics orders.

this updates the modeling process, enabling the calculation of harmonic winding functions ($\lambda_{win,\beta}$), as illustrated in (11):

$$
\left.\begin{aligned}
N_{thp} &= N_{Tph}/(P \times \beta) \\
\lambda_{win,\beta}(\alpha_s) &= \lambda_{win}(\beta \cdot \alpha_s)/\beta
\end{aligned}\right\}
$$
(11)

Therefore, the speed at which the revolving flux generated by the βth space harmonics rotates is $(1/\beta)$ times the fundamental synchronous speed of the induction motor and the direction of rotation is decided by the order of the space harmonics. In this context, when space harmonics intersect with higher-order time harmonics, especially when they are in the same harmonic order as the space harmonics, the resulting rotating magnetic fields also rotate at the fundamental synchronous speed of the motor therefore having a direct impact on the machine's average torque. Conversely, when there is interaction between space and time harmonics of unequal orders, it leads to torque ripples as their synchronous speeds differ from the fundamental speed.

The analysis of these harmonics is contingent upon the assumption of ignoring core MMF drops. In the following section, an examination of the effects stemming from core MMF drops is presented.

B. INTEGRATION OF CORE MMF DROPS CONSIDERING THE INFLUENCE OF SPACE AND TIME HARMONICS

The assumption of infinite core permeability in the traditional WF model became invalid due to the finite material's frequency-dependent permeability. As a result, the core MMF drops are no longer zero, instead, they become a function of the operating frequency and the level of the core flux densities. Since the flux density levels vary in different sections of the machines, the proper MMF drop calculations were conducted by sectionizing the stator and rotor cores as shown in Fig. 5. Therefore, Ampere's law is applied to redefine the net airgap MMF [$\Lambda_{net}(\alpha_s, t, f_s)$] as in (12):

$$
\left.\begin{aligned}
\Lambda_{net}(\alpha_s, \alpha_r, t, f_s) &= \Lambda_{win}(\alpha_s, t, f_s) - \Lambda_{atn}(\alpha_s, t, f_s) \\
where \quad \Lambda_{atn}(\alpha_s, t, f_s) &= \Lambda_{atn\_sta}(\alpha_s, t, f_s) \\
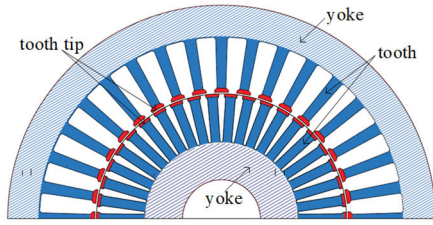&\quad + \Lambda_{atn\_rot}(\alpha_s, t, f_s)
\end{aligned}\right\}
$$
(12)

FIGURE 5. Stator and rotor core sections of IM for MMF drop calculations.

FIGURE 7. Core flux density variation over time with minor flux density loops.

where $\Lambda_{atn}(\alpha_s, t, f_s)$ represents the net total MMF drops at the core areas, which is due to the combined core MMF drops at the core sections: teeth, tooth, and yoke areas of the stator, $\Lambda_{atn\_sta}(\alpha_s, t, f_s)$ and rotor, $\Lambda_{atn\_rot}(\alpha_s, t, f_s)$ calculated along the stator reference axis and against time, which then considered the rotor movement over time.

Since magnetic field intensity, H, represents MMF drops per unit length, the MMF drops can be understood by examining the B-H characteristics of core materials. As a result, the core flux densities can be used as a direct means to estimate the frequency-dependent MMF drops of each core section, following the material's B-H characteristics, as illustrated in Fig. 6 and multiplying the readings by their respective mean magnetic path length (l_{mean}).
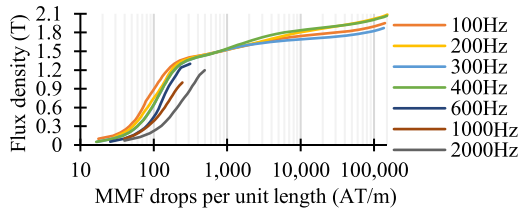

FIGURE 6. B-H characteristics of M19–29G laminations at sample frequencies [26].

In addition, assuming the flux passing through each section is concentrated and uniformly distributed in each section with no losses, the mean flux densities within the sections $B_{sec}(\alpha_s, t)$, are calculated as in (13). These calculations employ the surface integral of the corresponding flux density at the airgap calculated using the proposed modifications and it is necessary to consider the flux density in half of the stator and rotor's pole sections for yoke sections:

$$B_{\text{sec}}(\alpha_s, t) = \int_0^{2\pi/(N_{ss}\text{or}N_{rr})} B_{ag}(\alpha_s, t) \cdot ds \bigg/ A_{\text{sec}} \quad (13)$$

where N_{ss}, N_{rr} and A_{sec} represents the number of stator and rotor slots and cross-sectional areas of each section where the flux is perpendicular respectively. Therefore, $\Lambda_{win}(\alpha_s, t, f_s)$ in (3) is replaced by the net airgap MMF, $\Lambda_{net}(\alpha_s, t, f_s)$, to calculate the more accurate airgap flux density, $B_{sta}(\alpha_s, t)$, of the machine, which accounts for the MMF drops.

According to the WF theory, the higher order time harmonics caused timely variation of the core sectional flux densities
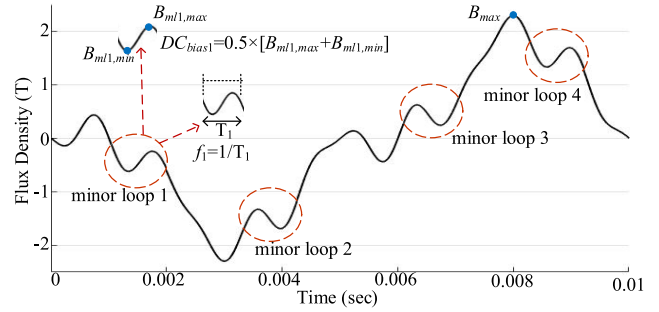
to be non-sinusoidal. This then followed the nearly sinusoidal variations with the sinusoidal excitations. Furthermore, these additional time-variant non-sinusoidal magnetic fields based on their magnitudes and phase shifts, create additional minor loops, which are influenced by their DC bias levels [25], as shown in Fig. 7. Therefore, this needs consideration in the calculation of core MMF drops under the non-sinusoidal core flux densities and using the proposed novel approach considering the alternative approaches:

■ Superposition principle by decomposing the non-sinusoidal core flux density waveform harmonics and calculating the MMF drops by treating them as sinusoidal waveforms with no minor loops. However, this causes the DC bias effects of each harmonic not to be considered and, therefore, zero DC bias causes MMF drops to be underestimated.

■ Therefore, the most appropriate approach is to consider the instantaneous core flux densities and the B-H characteristics including the major and minor flux density loops as well as the DC bias, which is calculated as half of the peak-to-peak flux density at minor loops as depicted in Fig. 7.

Determining the minor hysteresis loops requires experimentation that is not feasible at the IM design stages and the mathematical approaches are used for determining the hysteresis losses of the minor loops [25], which are not used to determine the MMF drops at the minor loops. Therefore, the alternative method proposed in this paper is to calculate the frequency of the minor loop (f_m) using its period (T_m), as shown in Fig. 7, and calculate the MMF drops using B-H curves for the minor loop frequencies as shown in Fig. 6. In addition, this method will also determine the instantaneous flux densities, which accounts for the DC biases.

Moreover, due to the high correlation between core flux densities and airgap flux density distribution within the linear segments of their respective B-H curves during operation, the corresponding MMF drops exhibit analogous trends to airgap flux densities. This resemblance extends to both space and time-harmonic orders. However, when saturation conditions come into play, the MMF drops deviate into non-linear patterns, consequently affecting the spatial and time harmonics

of airgap flux density and, therefore, the electromagnetic torque and its ripple content.

C. INTEGRATION OF CORE MMF DROPS INTO TORQUE CALCULATION

The process of calculating core MMF drops necessitates the examination of rapid fluctuations in flux densities which are primarily governed by the net airgap MMF and emerge from the collective impact of phase currents and their respective winding functions. Given the complex nature of this interdependence, accurately separating, and evaluating the distinct contributions of each phase to MMF drops is challenging. Consequently, integrating a traditional WF as described in (6), to calculate accurate self and mutual inductances poses significant challenges within this framework.

The situation becomes even more complex when the core flux densities reach the saturation region of non-linear *B-H* characteristics. Since energy stored in the magnetic field can be calculated based on the flux density [27], the proposed solution in this paper is to use the net energy, $W_{net}(\alpha_r, t)$, to calculate the net torque of the machine (τ_{em_net}), as shown in (14), while removing the energy associated with the MMF drops, $W_{atn}(\alpha_r, t)$, calculated based on the airgap magnetic flux density due to the MMF drops $B_{ag\_atn}(\alpha_s, t)$ as in (15).

$$\tau_{em\_net} = \frac{1}{2} \cdot \frac{P}{2} \cdot \frac{\partial \left[W_{coe}(\alpha_r, i(t)) - W_{atn}(\alpha_r, t) \right]}{\partial \alpha_r} \qquad (14)$$

$$\left. \begin{aligned} W_{atn}(\alpha_r, t) &= \frac{l_s}{2 \cdot (4\pi \times 10^{-7})} \int_0^{P\pi} B_{ag\_atn}^2(\alpha_s, t)\, d\alpha_s \\ B_{ag\_atn}(\alpha_s, t) &= (4\pi \times 10^{-7}) \times \Lambda_{atn}(\alpha_s, t, f_s) / \Delta_{eff}(\alpha_s, t) \end{aligned} \right\} \qquad (15)$$

Therefore, the proposed model considered the space harmonics due to the winding layout and the core MMF drops, while considering the time harmonics generated due to the PWM excitation and the total procedure of the proposed model used for torque calculation is shown in Fig. 8.

IV. IMPLEMENTATION AND VERIFICATION OF THE PROPOSED MODEL FOR THE INVERTER-FED INDUCTION MOTOR

The time-stepping approach, which converts the continuous functions into a discrete function is used in implementing the proposed model. Therefore, the machine's airgap perimeter is divided into *N* equidistant segments based on the sampling frequency. The discrete data points are extracted from each segment and employed in the subsequent calculations required for torque estimations, enabling the proposed model to be implemented in MATLAB.

For development and validation purposes, a laboratory prototyped SCIM with specific characteristics highlighted in Table 1 was utilized. The SCIM features a double-layer distributed winding layout with 3 slots per pole per phase and a coil span of 9. Additionally, the rotor bars are made of aluminum and have a pear-shaped design. For further validation FEA-based electromagnetic transient studies were conducted using the ANSYS Maxwell-Twin Builder co-simulation
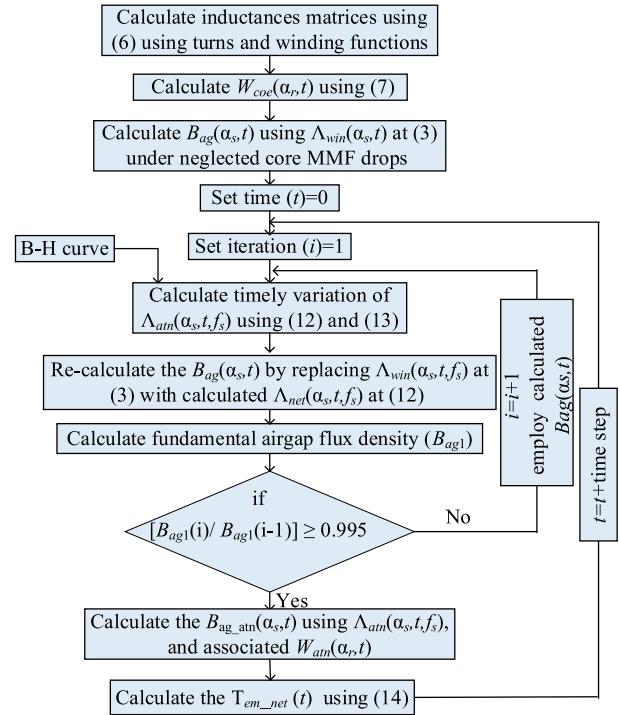

FIGURE 8. Flowchart of torque calculation procedure by the proposed model.

TABLE 1. Induction machine used in the investigations.

Parameter	Value	Parameter	Value
Electrical steel	M19–29G	Rated power	11 kW
D_{os}	157.2 mm	Peak power	36 kW
D_{is}	90.06 mm	Rated speed	2,905 rpm
D_{ir}	88.9 mm	Rated frequency	100 Hz
Airgap length	0.58 mm	P	4
l_{sh}	131.5 mm	DC link voltage	465 V
Turns per phase	72	Rated current (RMS)	35.4 A

using PWM excitation. Since lower-order current harmonics have prominent effects on the torque, the harmonics are limited to their 20th order. The harmonic spectrum of the current excitation for the selected speed points in the MTPA and FW regions under continuous power/torque conditions and MTPA operation point where the power/torque is 82% higher than that under continuous conditions are shown in Fig. 9. The latter case can be considered as a traction motor operating at the boost or between the continuous and peak operating conditions.

The accuracy of the proposed model is centered around the quality of two factors: (1) the turns and winding functions that calculate the inductances; and (2) the core MMF drops. This pertains to the direct influence of time harmonic effects, where the airgap MMF reflects the interaction of phase currents with the winding function, while the core MMF drops relate to timely variations in core flux densities.

Therefore, the optimal approach to validate the model's accuracy is calculating the inductances using (6), and integrating the combined influence of spatial and time-harmonic
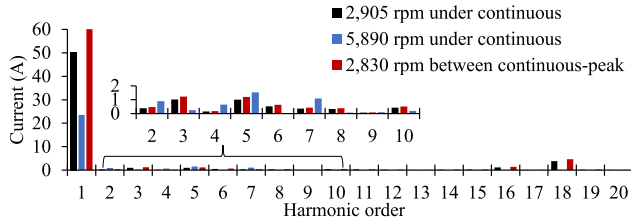
FIGURE 9. Current harmonic spectra for the simulated PWM-fed SCIM at different speeds under continuous power/torque and power/torque 82% higher than the continuous operation conditions.

effects through the airgap flux density calculated over time by considering the influence of core MMF drops, which is required to calculate $W_{atn}(\alpha_r, t)$ using (15). In such, Table 2, the averaged self- and mutual inductances of stator phase windings and the self-inductance of the rotor mesh loop, along with the root mean square of the mutual inductances between stator phase windings and rotor mesh loops, are presented with accuracies compared with FEA results.

TABLE 2. Comparison of calculated inductances by the proposed and traditional WF models with the FEA results.

Inductances	FEA	Proposed model	Traditional WF (TWF) model
Self stator winding [mH]	14.18	14.12 (99.6%)	11.5 (81.5%)
Mutual stator winding [mH]	-4.56	-4.20 (92.1%)	-6.2 (64%)
Mutual stator winding to rotor mesh loop [μH]	36.57	36.49 (99.8%)	31.2 (85.3%)
Self rotor mesh loop [μH]	3.28	3.01 (91.8%)	3.01 (91.8%)

Moreover, the impact of time harmonics and the influence of minor flux density loops on MMF drops can be verified using the time-varying airgap flux densities at different positions within the airgap. Such a comparison is presented in Fig. 10, utilizing identical PWM voltages as input parameters obtained from FEA simulations and flux densities obtained at the stator tooth section. Thus, speed points in the MTPA region operating under continuous and 82% higher power/torque than the continuous operation conditions were considered. Furthermore, Fig. 11 shows the FEA results of core flux densities for the above conditions and Table 3 provides estimates of selected prominent space harmonics of the airgap flux density over time in both the MTPA and FW regions.
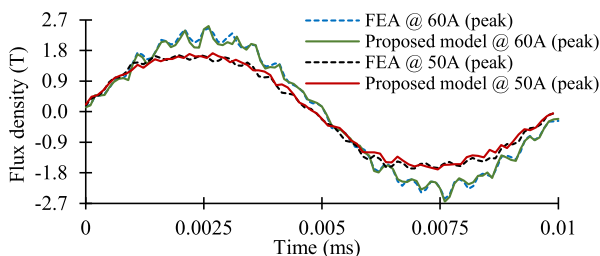

FIGURE 10. Comparison of average flux density in stator tooth region: (a) Continuous operation (50 A peak) at 2,905 rpm; (b) Power/torque 82% higher than the continuous operation (60 A peak) at 2,830 rpm.
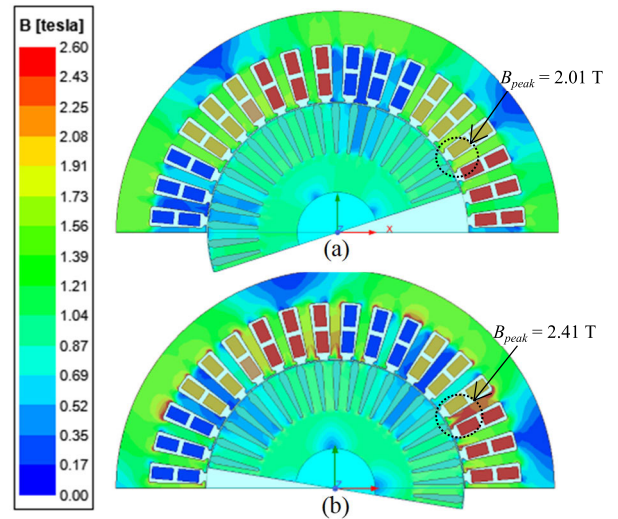

FIGURE 11. Core flux density distribution: (a) Continuous operation at 2,905 rpm; (b) Power/torque 82% higher than the continuous operation at 2,830 rpm.

TABLE 3. Comparison of averaged Airgap flux density comparisons of proposed and traditional WF models with FEA results.

Speed (rpm)	Harmonic order		FEA (T)	Proposed model (T)	TWF (T)
2,905 Continuous	Fundamental		0.835	0.824	1.091
	Stator slotting	17th	0.210	0.214	0.254
		19th	0.138	0.154	0.188
	Rotor slotting	20th	0.115	0.121	0.171
		22nd	0.126	0.163	0.173
5,890 Continuous	Fundamental		0.419	0.404	0.657
	Stator slotting	17th	0.110	0.116	0.169
		19th	0.072	0.081	0.128
	Rotor slotting	20th	0.064	0.072	0.117
		22nd	0.066	0.073	0.119
2,830 Between continuous & peak	Fundamental		0.871	0.854	1.183
	Stator slotting	17th	0.274	0.247	0.203
		19th	0.186	0.167	0.242
	Rotor slotting	20th	0.179	0.143	0.194
		22nd	0.186	0.151	0.201

According to Table 3, in MTPA and FW regions, under the continuous operation conditions, the accuracy of airgap density calculation in the proposed model is 98.2% and 96.4%, respectively, while the traditional WF model with neglected core MMF drops had accuracies of 70% and 67%, respectively. Furthermore, following a similar trend, the proposed model exhibits 98% accuracy when operating between continuous and peak operating conditions, while the traditional WF model accuracy drops further to 65%.

V. EXPERIMENTAL VALIDATION OF THE PROPOSED MODEL

To validate the accuracy of the proposed model in predicting average torque and torque ripple, a laboratory prototype of the aforementioned three-phase 11 kW SCIM was tested
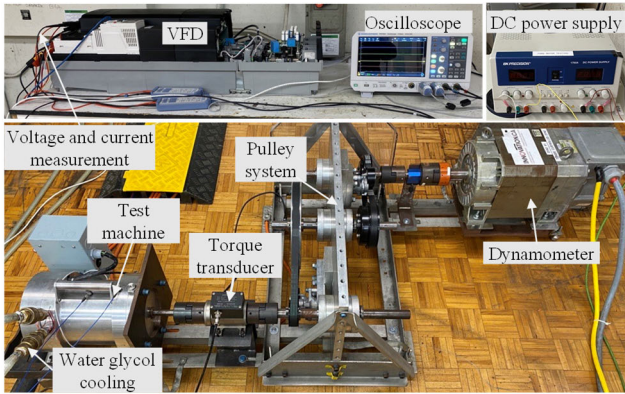
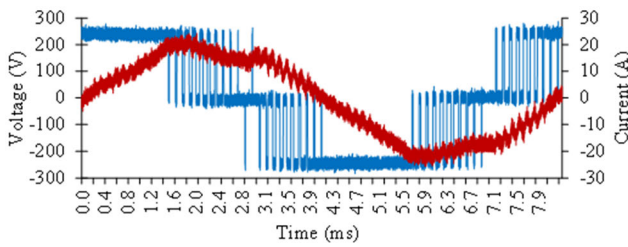**FIGURE 12. Experimental test setup to validate the proposed model.**

FIGURE 13. PWM voltage and current waveforms of Inverter-fed SCIM at 3,910 rpm and 11.5 Nm.
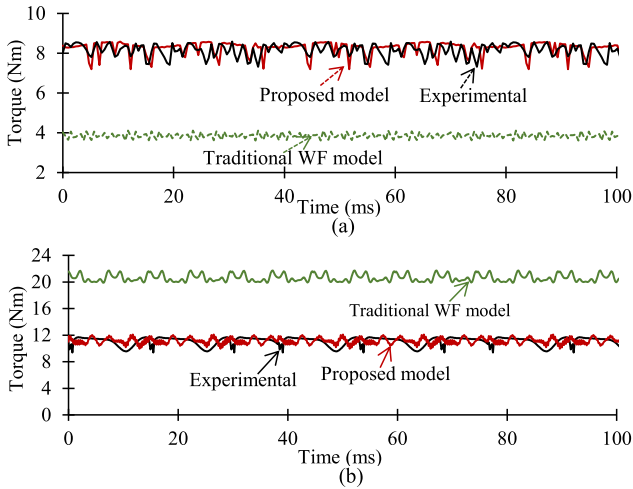

FIGURE 14. Comparison of torque profiles by different models with the measured one at different motor speeds. (a) At 1,500 rpm in the MTPA region; (b) At 3,910 rpm in the FW region.

FIGURE 15. Comparison of calculated and measured average torque and torque ripple for different speed conditions: (a) At 1,500 rpm in the MTPA region; (b) At 3,380 rpm in the FW region; (c) At 3,910 rpm in the FW region; (d) At 4,445 rpm in the FW region. (e) At 2,610 rpm and 2,400 rpm in the MTPA region @ 8% higher rated current, 54A(peak).

represented as τ_{em_max}, τ_{em_min}, and τ_{em_avg}, respectively.

$$\tau_{em\_ripple} = (\tau_{em\_max} - \tau_{em\_min}) \times 100\% / \tau_{em\_avg} \quad (16)$$

Figure 13 depicts the line-to-line PWM voltages and phase current obtained during a loaded condition at a speed of 3,910 rpm. In addition, Fig.14, presents a comparison of instantaneous torque profiles generated by the proposed model and traditional WF methods and Fig. 15 provides additional comparisons of average torques and torque ripples across various operating speeds and torque levels.

Referring to Fig. 15, the proposed model demonstrates high accuracy in predicting the average torque and torque ripple within the MTPA region, achieving 96.3% and 94.62%

in various operating conditions within both the MTPA and FW regions using the experimental test setup shown in Fig. 12. The motor's speed was controlled through a variable frequency drive (VFD) and loaded using a dynamometer. During these tests, the experimental torque profiles were compared with those predicted by the proposed method and the traditional WF method, which does not account for core MMF drops. Here, torque ripples (τ_{em_rip}) are determined using (16). The maximum, minimum, and average torque are
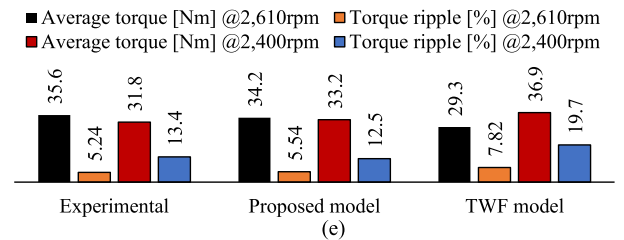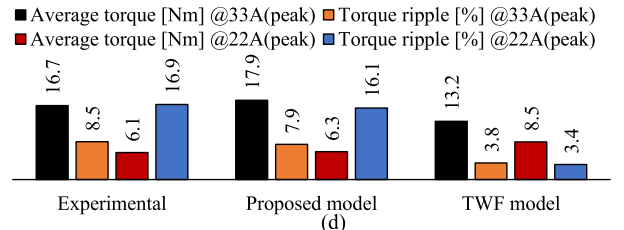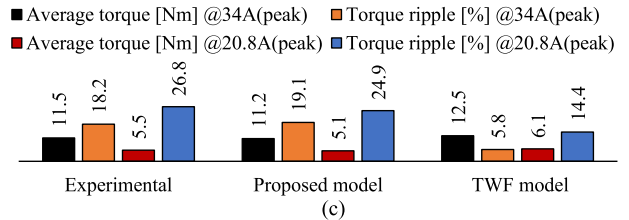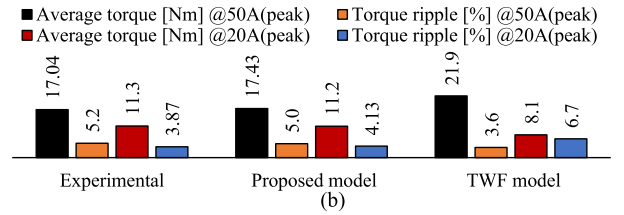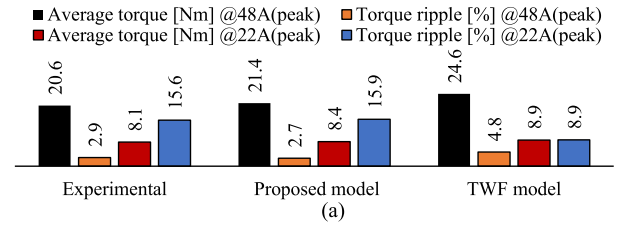
accuracy, respectively, while in the traditional WF model, the accuracies are reported as 84.5% and 49.1%, respectively, when compared to experimental data in the MTPA region.

Furthermore, within the FW region, the proposed model maintains its accuracies of 96.4% for average torque and 94.4% for torque ripple, compared to traditional WF models, these accuracies are significantly lower, 77.7% for average torque and 41.1% for torque ripple prediction when compared to experimental data. Hence, the enhanced torque calculation in the proposed model compared to the traditional WF can be attributed mainly due to the integration of time dependent core MMF drops considering minor flux density loop effects.

Furthermore, employing an Intel Core i5–7400 CPU operating at 3.3 GHz and that is equipped with 16 GB of RAM, the proposed model achieves an average computation time of 12.5 minutes. In contrast, the 2D FEA simulations, to reach a steady state in both the MTPA and FW regions consumed an average of 50 minutes with its default settings.

VI. CONCLUSION

This paper introduces a novel, computationally efficient magnetic field-based model for calculating electromagnetic torque and torque ripple in traction IMs design for EVs driven by PWM inverters, operating in both the MTPA and FW regions. The proposed model modifies the turns and winding functions considering the virtual winding occupied area, and the major and minor flux density loop effects resulting from the non-sinusoidal core flux densities emerged due to the combined effects of time and space harmonics are considered when calculating the core MMF drops. In addition, the calculated net energy serves as the solution to address the impracticality of isolating the MMF drops from each phase and this improvement enhanced the torque calculation of the proposed model. The results demonstrated the effectiveness of the proposed model, with an average accuracy improvement of 15.3% in torque and 49.4% in torque ripple calculations across a wider speed range when compared to the traditional winding function-based model. Consequently, the proposed model holds great promise for enhancing the precision of torque calculation, thereby playing a crucial role in the design of traction induction machines.

ACKNOWLEDGMENT

REFERENCES

[1] D. Zechmair and K. Steidl, "Why the induction motor could be the better choice for your electric vehicle program," *World Electric Vehicle J.*, vol. 5, no. 2, pp. 546–549, Jun. 2012.

[2] *Timeline: History of the Electric Car, U.S. Department of Energy*. [Online]. Available: www.energy.gov/timeline/timeline-history-electric-car

[3] R. Thomas, H. Husson, L. Garbuio, and L. Gerbaud, "Comparative study of the Tesla model S and audi e-Tron induction motors," in *Proc. 17th Conf. Electr. Mach., Drives Power Syst. (ELMA)*, Sofia, Bulgaria, Jul. 2021, pp. 1–6.

[4] F. Un-Noor, S. Padmanaban, L. Mihet-Popa, M. Mollah, and E. Hossain, "A comprehensive study of key electric vehicle (EV) components, technologies, challenges, impacts, and future direction of development," *Energies*, vol. 10, no. 8, p. 1217, Aug. 2017.

[5] N. Zhao and N. Schofield, "An improved induction machine design procedure for electric vehicle traction," in *Proc. 8th IET Int. Conf. Power Electron., Mach. Drives (PEMD)*, Apr. 2016, pp. 1–6.

[6] G. Joksimovic, P. Zajec, A. Tessarolo, V. Ambrožic, and A. Rihar, "Stator current spectral content of inverter-fed cage rotor induction motor," *IEEE Access*, vol. 10, pp. 23112–23121, 2022.

[7] D. Kouchih, R. Hachelaf, O. Benzineb, M. Tadjine, and M. S. Boucherit, "Diagnosis of cage induction motors subject to unbalanced supply voltage conditions including space and time harmonics," in *Proc. 14th Int. Conf. Sci. Techn. Autom. Control Comput. Eng.*, Dec. 2013, pp. 486–492.

[8] M. Ojaghi and S. Nasiri, "Modeling eccentric squirrel-cage induction motors with slotting effect and saturable teeth reluctances," *IEEE Trans. Energy Convers.*, vol. 29, no. 3, pp. 619–627, Sep. 2014.

[9] A. Mollaeian, E. Ghosh, H. Dhulipati, J. Tjong, and N. C. Kar, "3-D subdomain analytical model to calculate magnetic flux density in induction machines with semiclosed slots under no-load condition," *IEEE Trans. Magn.*, vol. 53, no. 6, pp. 1–5, Jun. 2017.

[10] A. Hemeida, M. M. Billah, K. Kudelina, B. Asad, M. U. Naseer, B. Guo, F. Martin, P. Rasilo, and A. Belahcen, "Magnetic equivalent circuit and Lagrange interpolation function modeling of induction machines under broken bar faults," *IEEE Trans. Magn.*, vol. 60, no. 3, pp. 1–4, Mar. 2024.

[11] E. Roshandel, A. Mahmoudi, S. Kahourzade, and W. L. Soong, "Saturation consideration in modeling of the induction machine using subdomain technique to predict performance," *IEEE Trans. Ind. Appl.*, vol. 58, no. 1, pp. 261–272, Jan. 2022.

[12] A. Mollaeian, A. Kundu, M. S. Toulabi, M. U. Thamm, S. Kim, J. Tjong, and N. C. Kar, "Fourier-based modeling of an induction machine considering the finite permeability and nonlinear magnetic properties," *IEEE Trans. Energy Convers.*, vol. 36, no. 4, pp. 3427–3437, Dec. 2021.

[13] T. A. Lipo, *Introduction To AC Machine Design*. Hoboken, NJ, USA: Wiley, 2017.

[14] A. C. Babu and J. Seshadrinath, "Stator inter-turn fault modelling and analysis on induction motor based on MCCM," in *Proc. Int. Conf. Sustain. Energy Future Electric Transp. (SEFET)*, Jan. 2021, pp. 1–6.

[15] B. Asad, T. Vaimann, A. Belahcen, A. Kallaste, A. Rassõlkin, and M. N. Iqbal, "Modified winding function-based model of squirrel cage induction motor for fault diagnostics," *IET Electric Power Appl.*, vol. 14, no. 9, pp. 1722–1734, Sep. 2020.

[16] Y. Cai, R. Ni, W. Zhu, and Y. Liu, "Modified approach to inductance calculation of variable reluctance resolver based on segmented winding function method," *IEEE Trans. Ind. Appl.*, vol. 59, no. 5, pp. 1–8, Sep. 2023.

[17] Q. Fu, S. Yue, B. He, and N. Fu, "Multiple coupled circuit modelling approach for squirrel cage induction machine under single-broken-bar fault with stator winding functions decomposed in d—q rotor reference frame," *IET Electric Power Appl.*, vol. 13, no. 7, pp. 889–900, Jul. 2019.

[18] V. Kindl, K. Hruska, J. Pechanek, J. Sobra, and B. Skala, "The effect of space harmonic components in the air gap magnetic flux density on torque characteristic of a squirrel-cage induction machine," in *Proc. 17th Eur. Conf. Power Electron. Appl.*, Sep. 2015, pp. 1–5.

[19] A. Marfoli, L. Papini, P. Bolognesi, and C. Gerada, "An analytical-numerical approach to model and analyse squirrel cage induction motors," *IEEE Trans. Energy Convers.*, vol. 36, no. 1, pp. 421–430, Mar. 2021.

[20] B. De Silva Guruwatta Vidanalage, M. Sedigh Toulabi, T. Stachl, A. Lombardi, J. Tjong, and N. C. Kar, "Winding function-based analytical modeling of core loss in an induction machine considering slotting effects and the frequency-dependent B-H curve characteristics," *IEEE Trans. Magn.*, vol. 58, no. 8, pp. 1–6, Aug. 2022.

[21] A. Ghoggal, S. E. Zouzou, M. Sahraoui, H. Derghal, and A. Hadri-Hamida, "A winding function-based model of air-gap eccentricity in saturated induction motors," in *Proc. XXth Int. Conf. Electr. Mach.*, Sep. 2012, pp. 2739–2745.

[22] A. Ghoggal and A. H. Hamida, "Transient and steady-state modelling of healthy and eccentric induction motors considering the main and third harmonic saturation factors," *IET Electric Power Appl.*, vol. 13, no. 7, pp. 901–913, Jul. 2019.

[23] B. Ge, W. Liu, J. Dong, and M. Liu, "Extending winding function theory to incorporate secondary effects in the design of induction machines and drives," *IEEE J. Emerg. Sel. Topics Power Electron.*, vol. 10, no. 2, pp. 1915–1924, Apr. 2022.

[24] F. Briz, M. W. Degner, J. M. Guerrero, and P. Garcia, "Stator windings fault diagnostics (Don't short) of induction machines operated from inverters and soft-starters using high-frequency negative-sequence currents," *IEEE Trans. Ind. Appl.*, vol. 45, no. 5, pp. 1637–1646, Sep. 2009.

[25] R. Kumar and P. Kumar, "Core loss estimation for an inverter-fed induction motor with more accurate realisation of material non-linearity and impact of hysteresis minor loops," *IEEE Trans. Energy Convers.*, vol. 37, no. 1, pp. 327–336, Mar. 2022.

[26] (2024). *NGO Magnetic Steel*. [Online]. Available: www.magweb.us

[27] J. Pyrhonen, T. Jokinen, and V. Hrabovcova, *Design of Rotating Electrical Machines*. Hoboken, NJ, USA: Wiley, 2008.

ANTHONY LOMBARDI received the Ph.D. degree in mechanical engineering from Toronto Metropolitan University (formerly Ryerson University), in 2015.

He was a NSERC Postdoctoral Fellow with the Materials Science and Engineering Department, University of Toronto, from 2015 to 2017, focusing on casting, heat treatment, and advanced materials characterization of Al alloys. He has been a Research and Development Engineering Specialist for Nemak's U.S./Canada Business Unit, since 2017, and his role is to seek novel methods for advancing quality, manufacturability, and performance of Nemak's product line and development of new lightweight materials with improved mechanical, thermal, and electrical properties. He has over 15 years of hands–on metal casting and heat-treating expertise in Al and Mg alloy development and has over 45 peer-reviewed publications, one granted patent, and one pending patent in this area.

JIMI TJONG received the B.Sc., M.Sc., and Ph.D. degrees in mechanical engineering from the University of Windsor, Windsor, ON, Canada, in 1980, 1984, and 1993, respectively. He is currently a retired Technical Leader and the Manager of the Ford Powertrain Engineering with the Research & Development Centre. He is also an Adjunct Professor with the University of Windsor, University of Toronto, Toronto, ON, Canada, and McMaster University, Hamilton, ON, Canada. His research interests include production and comprehensive design validation of components and systems for conventional and electrified vehicles and optimization of automotive test systems for cost, performance, and compatibility.

BUDDHIKA DE SILVA GURUWATTA VIDANALAGE (Graduate Student Member, IEEE) received the B.Tech. degree in electrical engineering from The Open University of Sri Lanka, Nawala, in 2013, and the M.Sc. degree in electrical engineering from the University of Manitoba, Winnipeg, MB, Canada, in 2018. He is currently pursuing the Ph.D. degree with the Centre for Hybrid Automotive Research and Green Energy (CHARGE), Department of Electrical and Computer Engineering, University of Windsor. His research interests include design, modeling, optimization, analysis of electric machines for electric vehicle applications, testing, and performance analysis of motor drives.

He was a recipient of many awards, including the E. W. Karunaratne Memorial Award, in 2013, for the best undergraduate project in electrical engineering, organized by the Institute of Engineers Sri Lanka (IESL), and the Dr. O. P. Kulshreshtha Gold Medal for the best student in the Bachelor of Technology (Engineering) Degree Program, in 2011 and 2012, from The Open University of Sri Lanka.

NARAYAN C. KAR (Senior Member, IEEE) received the B.Sc. degree in electrical engineering from Bangladesh University of Engineering and Technology, Dhaka, Bangladesh, in 1992, and the M.Sc. and Ph.D. degrees in electrical engineering from Kitami Institute of Technology, Hokkaido, Japan, in 1997 and 2000, respectively. He is currently a Professor with the Electrical and Computer Engineering Department, University of Windsor, Canada, where he also holds the Tier 1 Canada Research Chair in electrified vehicles. He is also the Founder and the Director of the Centre for Hybrid Automotive Research and Green Energy (CHARGE), University of Windsor. His research interests include electric machine and drive design, optimization, and testing for electric vehicle application. His research program is funded by multiple funding agencies, including the Government of Canada and automotives OEM and tiered suppliers.

• • •